

# HERSCHEL OBSERVATIONS AND UPDATED SPECTRAL ENERGY DISTRIBUTIONS OF FIVE SUNLIKE STARS WITH DEBRIS DISKS

SARAH E. DODSON-ROBINSON<sup>1</sup>, KATE Y. L. SU<sup>2</sup>, GEOFF BRYDEN<sup>3</sup>, PAUL HARVEY<sup>4</sup>, JOEL D. GREEN<sup>4,5</sup>

*Draft version October 6, 2016*

## ABSTRACT

Observations from the *Herschel* Space Observatory have more than doubled the number of wide debris disks orbiting Sunlike stars to include over 30 systems with  $R > 100$  AU. Here we present new *Herschel* PACS and re-analyzed *Spitzer* MIPS photometry of five Sunlike stars with wide debris disks, from Kuiper belt size to  $R > 150$  AU. The disk surrounding HD 105211 is well resolved, with an angular extent of  $> 14''$  along the major axis, and the disks of HD 33636, HD 50554, and HD 52265 are extended beyond the PACS PSF size (50% of energy enclosed within radius  $4''.23$ ). HD 105211 also has a  $24\mu\text{m}$  infrared excess that was previously overlooked because of a poorly constrained photospheric model. Archival *Spitzer* IRS observations indicate that the disks have small grains of minimum radius  $a_{\text{min}} \sim 3\mu\text{m}$ , though  $a_{\text{min}}$  is larger than the radiation pressure blowout size in all systems. If modeled as single-temperature blackbodies, the disk temperatures would all be  $< 60$  K. Our radiative transfer models predict actual disk radii approximately twice the radius of a model blackbody disk. We find that the *Herschel* photometry traces dust near the source population of planetesimals. The disk luminosities are in the range  $2 \times 10^{-5} \leq L/L_{\odot} \leq 2 \times 10^{-4}$ , consistent with collisions in icy planetesimal belts stirred by Pluto-size dwarf planets.

## 1. INTRODUCTION

Observations from the *Herschel* Space Observatory have revealed a population of extrasolar debris disks with blackbody temperatures  $< 60$  K and peak flux densities at wavelengths near  $100\mu\text{m}$ . Photodetector Array Camera and Spectrograph (PACS; Pilbratt et al. 2010)  $100\mu\text{m}$  and  $160\mu\text{m}$  observations of the DUSt around NEArby Stars (DUNES) Sunlike targets reveal a debris disk incidence of 20%, up from 12% at the shorter *Spitzer* MIPS wavelengths (Eiroa et al. 2013). Far-IR observations are therefore opening up a new discovery space of disks more than 100 times more luminous than the Edgeworth-Kuiper belt, but too cold to detect at  $70\mu\text{m}$ .

We now know of over 30 disks with radii  $R > 100$  AU (Eiroa et al. 2010; Morales et al. 2013; Duchêne et al. 2014; Pawellek et al. 2014). Since even wide disks require active collisional cascades to replenish  $1 - 10\mu\text{m}$  grains (Burns et al. 1979), planetesimal formation must be a robust process even at very large distances from the star. Planet formation at 125-250 AU may even have proceeded as far as super-Earth mass (Kenyon & Bromley 2015). The wide dust disks revealed by *Herschel* and earlier (sub)millimeter/scattered light observations (e.g. Greaves et al. 1998; Ardila et al. 2004; Krist et al. 2005; Wyatt et al. 2005; Hines et al. 2007; Kalas et al. 2007a,b; Liseau et al. 2008; Krist et al. 2010; Golimowski et al. 2011) may be remnants of planetary systems that orbit Sunlike stars but are nevertheless very different than our

own: dynamical evidence indicates that the solar nebula was likely truncated between 80 and 100 AU due to photoevaporation or tidal interactions with nearby young stars (Kretke et al. 2012; Anderson et al. 2013). Here we present *Herschel* observations of five Sunlike stars with debris disks that transition from Kuiper Belt size to  $R > 150$  AU. We use the Debris Disk Simulator (Wolf & Hillenbrand 2005) to construct model SEDs and compare our disk radii, grain sizes, and luminosities with other debris disks orbiting Sunlike stars.

We begin with a discussion of target selection, observations, and data reduction (section 2). Next, we discuss the extended structure observed in our images: our targets include one well-resolved disk and three moderately extended sources (section 3). We then present the new *Herschel* and *Spitzer* photometry in section 4. Radiative transfer models of the disk spectral energy distributions (SEDs) follow in section 5, with conclusions and possible future work in section 6.

## 2. OBSERVATIONS AND DATA REDUCTION

We selected five Sunlike stars with debris disks discovered in *Spitzer* observations for *Herschel* follow-up. All targets have infrared excess emission seen in both *Spitzer* IRS observations at  $32\mu\text{m}$  (Dodson-Robinson et al. 2011; Chen et al. 2014) and in *Spitzer* MIPS observations at  $70\mu\text{m}$  (Beichman et al. 2006; Bryden et al. 2009). (HD 105211 also has a MIPS  $24\mu\text{m}$  excess, which was not realized at the time of publication (Beichman et al. 2006); see section 5.1 for more detail.) The observing strategy was designed to ensure detection in all *Herschel* PACS bandpasses. Based on the two detections at different wavelengths, Dodson-Robinson et al. (2011) fit single-temperature blackbody models to the *Spitzer* excess emission, which we extended to the *Herschel* PACS bandpasses. Exposure times were selected such that each target would be detected at the  $3\sigma$  level, where  $\sigma$  was the quadrature sum of the instrument noise

<sup>1</sup>Department of Physics and Astronomy, University of Delaware, 217 Sharp Lab, Newark, DE 19716; sdr@udel.edu

<sup>2</sup>Steward Observatory, Department of Astronomy, University of Arizona, 933 North Cherry Ave, Tucson, AZ 85721

<sup>3</sup>Jet Propulsion Laboratory, California Institute of Technology, 4800 Oak Grove Dr, Pasadena, CA 91109

<sup>4</sup>Astronomy Department, University of Texas, 2515 Speedway Dr, C1400, Austin, TX 78712

<sup>5</sup>Space Telescope Science Institute, 3700 San Martin Dr, Baltimore, MD 21218

and the predicted confusion noise reported in the Herschel Observers’ Manual<sup>6</sup>. (In reality, some of the sources have brighter  $160\mu\text{m}$  backgrounds than predicted, leading to detections with low significance or non-detections.)

Each observation consists of PACS medium-speed cross-scans separated in position angle by  $40^\circ$ . Program OT1\_sdodsonr\_1 includes simultaneous  $100\mu\text{m}/160\mu\text{m}$  observations of all targets as well as simultaneous  $70\mu\text{m}/160\mu\text{m}$  observations of HD 50554 and HD 105211. Observations are scan maps with eight scan legs of length  $3'$  and cross-scan step  $4''$ . We also obtained  $70\mu\text{m}/160\mu\text{m}$  observations of HD 50554, HD 52265, and HD 202206 from the Herschel Science Archive (program OT1\_amoromar\_1, PI A. Moro-Martín). Data reduction beginning with the Level 1 data cubes was performed using the Herschel Interactive Processing Environment version 12.1.0 (HIPE; Ott 2010). We used the HIPE implementation of the JScanam map-making algorithm (Graciá-Carpio et al. 2015) to combine scans and cross-scans into oversampled mosaics of  $1''$  per pixel at  $70$  and  $100\mu\text{m}$  and  $2''$  per pixel at  $160\mu\text{m}$ . The JScanam mapper removes the  $1/f$  noise that results in signal drifts without subtracting extended emission, which was an important consideration because some of our sources are not pointlike (see Section 3). However, JScanam also leaves point sources intact, so can be used for any type of target. Table 3 (located on the last page of this document) lists the targets in our sample and their Herschel Science Archive observation IDs. The table also includes luminosity and age estimates from the literature (McDonald et al. 2012; Chen et al. 2014; Bonfanti et al. 2015) and luminosity estimates from this work<sup>7</sup>. Figures 1, 2, 3, 4, and 5 show the final mosaics in each band for all targets.

### 3. EXTENDED STRUCTURE

Determining the spatial extent of the disks is important for selecting the correct aperture sizes for photometry. Examining the  $70\mu\text{m}$  and  $100\mu\text{m}$  mosaics in Figures 1, 2, 3, 4 and 5 suggests that the disks are not point sources, but instead have some extended structure. Figures 1, 2, 3, and 5 contain curves of growth for HD 33636, HD 50554, HD 52265, and HD 202206 showing encircled energy fraction as a function of circular aperture radius for the  $100\mu\text{m}$  (green) and, where available,  $70\mu\text{m}$  (blue) mosaics. For comparison, the dashed lines show curves of growth from the point source Vesta (Lutz 2010). For HD 33636, HD 50554, and HD 52265, the curves of growth are well below those of the Vesta PSF, indicating that the sources have extended structure. HD 50554 is elongated at both  $70\mu\text{m}$  and  $100\mu\text{m}$ , but has a small apparent position angle shift between the two bands. Fitting an elliptical Gaussian function to the source, we find a position angle (East of North) of  $54^\circ$  at  $70\mu\text{m}$  and  $51^\circ$  at  $100\mu\text{m}$ . The  $3^\circ$  difference is too small to conclusively indicate morphology changes between dust emitting at different wavelengths, but should be kept in

<sup>6</sup> Document HERSCHEL-HSC-DOC-0876

<sup>7</sup> We calculate luminosities based on  $V$ -band magnitudes using  $\frac{L_*}{L_\odot} = 2.512^{(M_\odot - M_*)}$ , where the variables  $M$  and  $L$  represent absolute magnitude and luminosity. We find better than 10% agreement between our luminosity calculations and the literature values and base all further analysis on our own luminosity calculations.

mind as a possible source of uncertainty in the photometry and SED fitting. HD 202206 is less well resolved than the other sources, but is still more extended than a point source. For some targets some cases the curves of growth turn downward instead of monotonically increasing with aperture size, indicating that the aperture has expanded to include pixels with negative flux densities. The photometric aperture must be kept smaller than the curve-of-growth turnover radius. HD 105211 (Figure 4) is clearly resolved in all PACS bands. The extended nature of our targets leads us to use larger photometric apertures than the faint-source sizes used by the DUNES team (Eiroa et al. 2013). We use  $12''$  as our nominal aperture size at  $70$  and  $100\mu\text{m}$  (see Section 4), which captures the extended emission yet avoids negative-valued pixels.

The upper-right panel of Figure 4 shows the deconvolved  $70\mu\text{m}$  image of HD 105211. Examination of a point source located in the  $70^\circ$  cross-scan, shown in the inset plots of the original image (upper left) and the deconvolved image, reveals the extent to which deconvolution has suppressed the trefoil PSF structure. Although our deconvolution procedure does not perfectly conserve flux, one can still see that most of the emission in the deconvolved image is concentrated in a narrow band indicating a nearly edge-on disk. We performed an elliptical Gaussian source fit on the original (not deconvolved)  $70\mu\text{m}$  image and found  $\sigma_x = 6.8''$  and  $\sigma_y = 3.9''$ , where the  $x$ -direction is East-West and the  $y$ -direction is North-South. The position angle is  $29.7^\circ$  East of North. Assuming a circular debris ring, the radius of the  $70\mu\text{m}$ -emitting ring is approximately  $\sqrt{\sigma_x^2 + \sigma_y^2} = 7.9''$ , or 154 AU, in rough agreement with the SED fitting results (see section 5). The inner edge of the ring is not resolved, possibly due to the high inclination of the disk.

### 4. PHOTOMETRY

For all targets except for HD 105211, our aperture photometry is based on the PACS ipipe script `L3_pointSourceAperturePhotometry.py`<sup>8</sup>, which uses the HIPE tasks `annularSkyAperturePhotometry` and `photApertureCorrectionPointSource`. For HD 33636, HD 50554, and HD 202206, aperture sizes are  $12''$  at  $70\mu\text{m}$  and  $100\mu\text{m}$ , with background subtraction based on sky annuli of  $25 - 35''$ . For HD 52265 we use an  $8''$  aperture and an  $18 - 22''$  sky annulus at both  $70\mu\text{m}$  and  $100\mu\text{m}$  to exclude a bright source west of the target. At  $160\mu\text{m}$ , where confusion noise is most severe, we use a  $14''$  aperture and decrease the sky annulus to  $24 - 28''$  for HD 33636 and HD 202206. For HD 50554 at  $160\mu\text{m}$  we use an aperture of  $10''$  and a sky annulus of  $20 - 24''$  in order to avoid a nearby source. HD 52265 is undetected at  $160\mu\text{m}$  due to confusion. For the extended source HD 105211, we use the Aperture Photometry Tool (APT; Laher et al. 2012). We choose an elliptical aperture of semimajor axis  $18''$  and semiminor axis  $12''$  at an angle of  $30^\circ$  East of North. The sky annulus has major axis  $30 - 45''$  and minor axis  $20 - 30''$  at  $70$  and  $100\mu\text{m}$ , and major axis  $30 - 44''$  and minor axis  $20 - 29.3''$  at  $160\mu\text{m}$ . The elliptical aperture corrections

<sup>8</sup> Author: Markus Nielbock; available in HIPE through the ‘Scripts → PACS Useful Scripts’ menu

are based on Table 2 of Balog et al. (2014), which reports encircled energy fraction (EEF) as a function of circular aperture radius for each PACS filter. For an aperture with semimajor axis  $a$  and semiminor axis  $b$ , the multiplicative aperture correction  $A$  is

$$A = \frac{1}{\sqrt{\text{EEF}(a) \times \text{EEF}(b)}}. \quad (1)$$

For  $a = 18''$  and  $b = 12''$ , we find aperture corrections of 1.201 at  $70\mu\text{m}$ , 1.241 at  $100\mu\text{m}$ , and 1.384 at  $160\mu\text{m}$ .

Uncertainties have several components: Poisson noise from the source, sky background, PACS absolute flux calibration, and residual  $1/f$  noise that may elude the map-making algorithm. Since the pixels in each final mosaic are not native, but instead are reconstructed from multiple scans of the source, they are not independent and the method of estimating random noise as  $\sigma_{\text{sky}}\sqrt{N_{\text{pix}}}$  (where  $\sigma$  is the standard deviation of the sky flux and  $N_{\text{pix}}$  is the number of pixels in the aperture) does not work. Instead, the usual procedure for calculating the random component of the PACS-image error budget is to place apertures of the same size and shape used for the science target on the sky background and calculate the standard deviation of the aperture-corrected flux from each. Following Balog et al. (2014), we use six apertures placed evenly around the outer edge of the background sky annulus for all targets except HD 105211. The HD 105211 sky background is structured, with an extended bright source directly to the west of the disk (Figure 4; see especially the  $160\mu\text{m}$  image at the lower right). To estimate photometric error for HD 105211, we use 12 elliptical apertures placed randomly on the image, excluding the bright source. Finally, we include conservative estimates of the systematic errors—both from absolute flux calibration and repeatability—of 7% of the source flux (Balog et al. 2014). Quoted uncertainties are the quadrature sum of the random and systematic errors. Table 1 lists the measured PACS flux densities.

As a consistency check, we compare our PACS  $70\mu\text{m}$  flux densities with *Spitzer* MIPS  $70\mu\text{m}$  observations. Published values come from the catalog of Chen et al. (2014), which includes photometry from a variety of literature sources. We also present new photometry of both the  $24\mu\text{m}$  and  $70\mu\text{m}$  images based on the MIPS team in-house pipeline (Gordon et al. 2005; Su et al. 2010)<sup>9</sup>. MIPS did not observe HD 202206 at  $24\mu\text{m}$ . We use PSF extraction to find  $24\mu\text{m}$  flux densities for the remaining targets. All targets have MIPS  $70\mu\text{m}$  data. We use PSF extraction to measure  $70\mu\text{m}$  flux densities for all targets except HD 105211, for which we use an aperture with radius  $35''$  and a sky annulus of  $39 - 65''$ .

Table 1 lists the MIPS flux densities for each target. The two MIPS  $24\mu\text{m}$  analysis pipelines yield flux densities that are consistent at the  $1-2\sigma$  level, though there is a clear discrepancy in how the error bars are computed for HD 105211. The MIPS  $70\mu\text{m}$  flux densities from the two pipelines are fully consistent for each source except HD 105211. The low HD 105211  $70\mu\text{m}$  flux density of 474 mJy reported by Beichman et al. (2006) is probably due to their choice to use a uniform aperture radius of

$1.5$  camera pixels ( $7''/8$ ) for the entire survey. Since the spatial extent of the HD 105211 disk in our PACS  $70\mu\text{m}$  images is  $> 14''$  on the major axis, Beichman et al. (2006) may have underestimated the flux density. The remaining PACS and MIPS  $70\mu\text{m}$  fluxes are consistent at the  $1\sigma$  level, indicating good agreement between the *Spitzer* and *Herschel* fluxes.

As a final test of our photometry pipeline, we measure fluxes from the PACS calibrator star  $\alpha$  Ceti (HD 18884). We use scan/cross-scan AOR pairs 1342212853/1342212854 ( $100/160\mu\text{m}$ ; observing day 614) and 1342203030/1342203031 ( $70/160\mu\text{m}$ ; observing day 457). The scan/cross-scan pairs were processed with the same JScanam map-making script as the science observations. We then performed photometry with the nominal aperture and sky annuli used for HD 33636, HD 52265, and HD 202206 (our compact, uncrowded targets). Our results match those of the instrument team (Table 12 Balog et al. 2014) to within 1% at all wavelengths, demonstrating the high accuracy of our data pipeline for pointlike sources with clean backgrounds (see Section 5 for caveats about the HD 105211 observations).

In the next section we combine *Spitzer* and *Herschel* observations to extend SED coverage to the peak wavelengths of dust emission, using a radiative transfer model to derive dust properties.

## 5. SPECTRAL ENERGY DISTRIBUTIONS

The disks in this study are cold enough that observations at  $70\mu\text{m}$  and shorter wavelengths probe only the increasing side of the  $F_\nu(\lambda)$  curve. The *Herschel* photometry extends coverage to the peak and the decreasing side of  $F_\nu(\lambda)$ . We use the Debris Disk Simulator (DDS)<sup>10</sup> (Wolf 2003; Wolf & Hillenbrand 2005) to fit SED models to the *Spitzer* IRS/MIPS and *Herschel* PACS photometry. The DDS takes as input a stellar spectrum, an inner and outer radius for the dust ring, a dust mass, an analytical or numerical description of the dust number density  $n(r)$  (where  $r$  is the distance from the star), and a grain size distribution of the form  $n(a) \propto a^{-q}$ ;  $a_{\text{min}} \leq a \leq a_{\text{max}}$  ( $a$  is the grain radius and we set  $q = 3.5$ ). The assumption of a power-law grain size distribution is reasonable for the larger grains, but dynamical models that include loss processes such as Poynting-Robertson drag predict that for grains with  $a \lesssim 10\mu\text{m}$ , the size distribution turns over so that the grain abundance *increases* with radius (Wyatt et al. 2011; Kenyon & Bromley 2016). Since the far infrared-emitting dust grains are most likely part of a collisional cascade that includes large grains, we set  $a_{\text{max}} = 1$  mm for all models. Larger particles would be present, but the grain size distribution is so steep that the larger grains would contribute only  $(a_{\text{max}}/1\mu\text{m})^{-1/2} = 3\%$  of the total thermal emission. The DDS also allows the user to set the chemical composition of the grains; here we assume 100% astronomical silicate (Laor & Draine 1993). Since we do not explore the composition options, our model SEDs are plausible but not unique. In particular, the grains could have organic components or ice mantles, though ice would eventually succumb to photodesorption. However, the small number of spectral data points

<sup>9</sup> New photometry presented in Table 1 is labeled “Su et al. (2010)” under Analysis Method.

<sup>10</sup> [www1.astrophysik.uni-kiel.de/dds/](http://www1.astrophysik.uni-kiel.de/dds/)

that cover the bulk of the disks’ emission do not warrant extremely flexible fits.

The parameters we explore are minimum grain size  $a_{\min}$ , the debris ring’s distance from the star  $R$ , the width of the debris ring  $\sigma$  (assuming a Gaussian number-density profile centered at  $R$ ), and the mass of grains smaller than  $a_{\max} = 1$  mm. Input star spectra are Atlas9 model photospheres (Kurucz 1992) originally fitted by Dodson-Robinson et al. (2011), based on *Hipparcos/Tycho BT* and *VT* magnitudes (Perryman et al. 1997; Høg et al. 2000) and 2MASS *JHK* magnitudes (Cutri et al. 2003). Where available, we added *RI* photometry from Bessell (1990). We also checked for consistency between the Dodson-Robinson et al. (2011) model photospheres and the allWISE photometry (Wright et al. 2010; Cutri et al. 2013) and found good agreement. The allWISE photometry was particularly important for HD 105211, which has conflicting photosphere models in the literature due to poor-quality 2MASS photometry; and for HD 52265, which has a poor-quality 2MASS *J* magnitude. Table 2 lists the fitted parameters for each SED, and Figures 6-10 show the model SEDs. We begin our discussion of SEDs with a detailed look at the photosphere model and mid-IR photometry of HD 105211, which requires extra care because of the imprecise 2MASS data, then move on to the ensemble properties of our disks.

### 5.1. HD 105211 Mid-IR Photometry and Photosphere

HD 105211 is bright enough to have saturated the 2MASS detectors, so the *JHK* flux densities have  $> 20\%$  errors. The near-infrared data is important for constraining the Rayleigh-Jeans side of the spectrum, as the turnover to an  $F_{\nu} \propto \lambda^{-2}$  power law happens in the *H* band for HD 105211. A further issue is that the SIMBAD database identifies HD 105211 as a spectroscopic binary, though Eggleton & Tokovinin (2008) find that a single star is the most probable configuration. If HD 105211 is a binary, a single photosphere model might not accurately reproduce the emission from both components. Beichman et al. (2006) presented the first *Spitzer* observations of HD 105211, reporting an infrared excess at  $70\mu\text{m}$  but not at  $24\mu\text{m}$ . Their measured excess was based on a model photosphere with  $T_{\text{eff}} = 6600$  K, which was fit to *BVJHK* photometry and predicted a photospheric flux density of 363.4 mJy at  $24\mu\text{m}$ . Saffe et al. (2008) then measured  $T_{\text{eff}} = 6900$  K from spectroscopy, which agrees with the optical spectral type F2 V of Gray et al. (2006). Dodson-Robinson et al. (2011) added *RI* photometry from Bessell (1990) to the photospheric fit constraints, which yielded a best-fit photosphere model with  $T_{\text{eff}} = 7250$  K. Moving to the new, hotter photosphere model yields a higher near-IR/mid-IR flux ratio and a lower predicted photospheric  $24\mu\text{m}$  flux density of 321.9 mJy. Based on the Dodson-Robinson et al. (2011) model photosphere and our re-reduction of the MIPS data, HD 105211 has a  $13\sigma$  excess at  $24\mu\text{m}$  (see Table 1). Chen et al. (2014) computed a third model photosphere with a predicted  $24\mu\text{m}$  flux of 347.1 mJy, which combined with the new MIPS re-reduction yields a  $7\sigma$  excess at  $24\mu\text{m}$ . The allWISE W1 photometry best corresponds to the Dodson-Robinson et al. (2011) photosphere model, with a monochromatic  $3.35\mu\text{m}$  flux density only  $0.11\sigma$  higher than the model. As the star is satu-

rated in W2 (see Figure 9), we do not re-fit the model photosphere with the allWISE data added. We adopt the Dodson-Robinson et al. (2011) photosphere model for this work, but note that the accuracy of the spectral type and effective temperature would benefit from additional data. James (2013) find an intrinsic scatter of about two spectral subtypes in a cross-correlation analysis of their spectral library—for example, the spectrum of a star typed F8 V might best match the F6 V template spectrum—a level of uncertainty consistent with the differences between the analyses of Dodson-Robinson et al. (2011), Chen et al. (2014), Saffe et al. (2008), and Gray et al. (2006).

There is still concern about the IRS data, however. Since slit loss led to 5-10% flux density underestimates in IRS, Dodson-Robinson et al. (2011) calculated absolute flux densities by assuming that the shortest-wavelength data points of the SL1 module (beginning at  $7.58\mu\text{m}$ ) traced the photosphere. The LL2 and LL1 data were then spliced to the SL1 data so as to make a continuous function. However, the data at the long-wavelength end of LL2 ( $19 - 20\mu\text{m}$ ) have large error bars, and there appears to be a drop in fractional excess flux at the short-wavelength end of LL1 ( $> 20\mu\text{m}$ ; see Figure 2 of Dodson-Robinson et al. (2011)). It is possible that HD 105211 has multiple debris belts, which would account for the rise and fall of fractional excess at  $19 - 20\mu\text{m}$ , but the IRS data are not conclusive. What is concerning is that the IRS data differ from the allWISE W4 data (after conversion to monochromatic flux at  $22.1\mu\text{m}$ ) by  $\sim 5\sigma$ . (Beichman et al. (2006) and our MIPS re-reduction disagree on the errors in the MIPS  $24\mu\text{m}$  flux, but adopting  $\sigma = 22.5$  mJy from Beichman et al. (2006), our IRS  $24\mu\text{m}$  flux density is consistent with the MIPS data.) The disagreement between W4 and IRS may be due to the W4 color correction; the bandpass is broad and the SED is no longer photospheric. The IRS, allWISE, and MIPS data all indicate an infrared excess at  $22 - 24\mu\text{m}$ , but the level of excess is still open to debate.

We also have some concerns about the photometry at  $160\mu\text{m}$  due to the bright source east of the target, which may have led to over-subtraction of the sky background. We find it difficult to reproduce the “peakiness” of the SED at  $100\mu\text{m}$ ; dust models that fit the  $32/70\mu\text{m}$  flux ratio tend to over-predict the  $160\mu\text{m}$  flux density and models that reproduce the  $70/100\mu\text{m}$  flux ratio tend to under-predict the  $32\mu\text{m}$  flux density. A low abundance of grains near the minimum size, as suggested by collisional cascade models that predict non power-law size distributions (Wyatt et al. 2011; Kenyon & Bromley 2016), might improve the SED fit by decreasing the  $32/70\mu\text{m}$  flux ratio. The SED model shown in Figure 9 is a compromise between the opposing constraints at 32 and  $70\mu\text{m}$ . Reducing the maximum grain size that contributes to the emission from the 1 mm assumed for all disks could reduce the predicted  $160\mu\text{m}$  flux density, but we doubt the physical realism of any model that includes small grains without a continuous size distribution extending to macroscopic grains. The uncertainties in the PACS and MIPS photometry (section 4) and the underlying photosphere model must be kept in mind when discussing the dust properties. Based on the infrared excess at both  $24\mu\text{m}$  and  $70 - 160\mu\text{m}$ , we strongly suggest follow-up observations of HD 105211 with both JWST and ALMA.

## 5.2. Dust Properties

We now turn our attention to the properties of the dust in our systems, including the disk radius, minimum grain size, location of dust relative to the parent planetesimal population, and possibility of planet sculpting. First, we find that all of the dust SEDs peak between  $80\mu\text{m}$  and  $120\mu\text{m}$ , which is typical of debris disks from the DUNES program (Krivov et al. 2013). We do not find any sources that are brighter at  $160\mu\text{m}$  than  $100\mu\text{m}$ , a feature which could indicate either a background galaxy in the beam (Gáspár & Rieke 2014) or a disk of unstirred, primordial grains (Krivov et al. 2013). We diagnose the presence of superheated small grains by computing the parameter  $\Gamma = R/R_{\text{BB}}$ , the ratio of the disk radius from our SED models (in which dust temperature depends on grain size) to the disk radius if only blackbody grains were present:

$$T_{\text{BB}} = 5100 \text{ K} (1 \mu\text{m}/\lambda_{\text{max}}) \quad (2)$$

$$R_{\text{BB}} = \left( \frac{278 \text{ K}}{T_{\text{BB}}} \right)^2 \left( \frac{L_*}{L_\odot} \right)^{1/2} \text{ AU}. \quad (3)$$

In equation 3,  $T_{\text{BB}}$  is the temperature of blackbody grains,  $\lambda_{\text{max}}$  is the wavelength of maximum emission, and  $R_{\text{BB}}$  is the radius of the ring of blackbody dust. The disks in our sample have  $1.7 < \Gamma < 2.7$  (Table 2). Although four out of five of our disks are not well enough resolved to measure disk sizes directly from the images, our SED-based values of  $\Gamma$  agree well with studies of resolved debris disks (e.g. Rodriguez & Zuckerman 2012; Booth et al. 2013). Each disk must contain a population of small grains that do not emit efficiently at  $\sim 100\mu\text{m}$  wavelengths and so heat above the local blackbody temperature. Given the presence of small grains, our sources are most likely self-stirred or planet-stirred planetesimal belts with grain-producing collisional cascades, which is consistent with our assumption of  $q = 3.5$  (Pan & Schlichting 2012; Matthews et al. 2014).

Dodson-Robinson et al. (2011) estimated blackbody temperatures  $T_{\text{BB}}$  for our target stars based on *Spitzer* IRS and MIPS (spectro)photometry at  $32\mu\text{m}$  and  $70\mu\text{m}$ . For the warmer debris systems HD 50554, HD 52265, and 105211, their estimates agree well with ours. For HD 33636 and HD 202206, the peak flux density is much redder than  $70\mu\text{m}$  and the *Herschel* observations indicate colder blackbody temperatures than the *Spitzer*-based photometry. We emphasize that the SEDs modeled here are not based on blackbody grains—our comparison between single-temperature blackbody models simply highlights the importance of far-IR photometry in characterizing the debris rings.

The *Spitzer* IRS spectra provide the best constraint on minimum grain size. In the Rayleigh regime, where  $2\pi a \ll \lambda$ , the grain opacity  $\kappa$  declines with wavelength as  $\kappa \propto \lambda^{-\beta}$ , where  $\beta = 2$  for simple conductors and insulators (Draine 2006). At  $32\mu\text{m}$ , the center of the spectral window used by Dodson-Robinson et al. (2011) to detect infrared excesses,  $2\pi a = \lambda$  for  $\lambda = 5.1\mu\text{m}$ . We find that the lack of *Spitzer* IRS fractional excesses at  $20\mu\text{m}$  (with the exception of HD 105211) and the small, though detectable, excesses at  $32\mu\text{m}$  exclude grains smaller than  $\sim 3 - 4\mu\text{m}$ , as such grains would emit efficiently from  $20 - 30\mu\text{m}$ . The minimum grain sizes predicted by

our best-fit model SEDs are in good agreement with the Pawellek & Krivov (2015) SED-based measurements from 32 objects (see their Figure 4): all of their target stars with  $L_\odot < L_* \leq 10L_\odot$  have  $\sim 2\mu\text{m} < a_{\text{min}} < \sim 10\mu\text{m}$ .

There is, of course a degeneracy between  $R$  and  $a_{\text{min}}$ . As an example, one model of the HD 50554 debris disk has  $R = 40$  and  $a_{\text{min}} = 5.5\mu\text{m}$ , while another has  $R = 45$  AU and  $a_{\text{min}} = 4.5\mu\text{m}$ ; the difference between their reduced  $\chi^2$  statistics is only 0.2. Yet the value of  $R$  from the SED of the resolved source HD 105211 is in rough agreement with the measured size from the image ( $175$  AU vs.  $154$  AU), suggesting that we have broken the degeneracy for at least one source. Indeed, we find it difficult to reproduce the measured  $32/70\mu\text{m}$  flux ratios without setting a minimum grain size larger than the radiation-pressure blowout size of (Burns et al. 1979)

$$a_{\text{rp}} \geq \frac{6L_* \langle Q_{\text{pr}}(a) \rangle}{16\pi GM_* c \rho}, \quad (4)$$

where  $L_*$  and  $M_*$  are the star luminosity and mass,  $\langle Q_{\text{pr}}(a) \rangle$  is the radiation pressure coupling coefficient averaged over all frequencies in the stellar spectrum, and  $\rho$  is the particle density ( $2.2 \text{ g cm}^{-3}$  for astronomical silicate). In the geometric optics limit where  $\langle Q(a) \rangle = 1$  for all values of  $a$ , we find blowout size limits of  $0.5 - 2.2\mu\text{m}$  for the range of star luminosities and spectral types in our sample. Intriguingly, Pawellek et al. (2014) and Pawellek & Krivov (2015) show that  $a_{\text{min}}/a_{\text{rp}}$ , the ratio of the true minimum grain size to the minimum predicted value from equation 4 (now with  $\langle Q_{\text{pr}}(a) \rangle$  calculated self-consistently from grain optical properties), is a decreasing function of stellar luminosity, approaching unity for A-type stars but with larger values for Solar-type stars. Our results agree well with theirs: the most luminous star in our sample, HD 105211 with  $L_*/L_\odot > 7$ , has  $a_{\text{min}}/a_{\text{rp}} \sim 2$ , while our least luminous star, HD 33636 with  $L_*/L_\odot = 1.05$ , has  $a_{\text{min}}/a_{\text{rp}} \sim 6$ .

We suggest that our *Herschel* observations most likely trace dust near the “birth ring” (Strubbe & Chiang 2006), where the source planetesimals reside. The largest grains that can emit like blackbodies at  $160\mu\text{m}$  have radii set by  $2\pi a \approx \lambda$ , such that  $a \approx 25\mu\text{m}$ . The lifetime  $\tau$  of a grain against Poynting-Robertson drag is

$$\tau = \frac{16\pi c^2 \rho R^2 a}{3L_*}, \quad (5)$$

where  $c$  is the speed of light. For  $25\mu\text{m}$  grains, we find  $0.2\text{Gyr} \leq \tau \leq 2\text{Gyr}$  for all of the disks in our sample. The quantity star age/ $\tau$  for  $25\mu\text{m}$  grains is between 0.7 and 6.5 for all systems except one; HD 50554 has age estimates that differ by a factor of 10 (3.3 Gyr from Bonfanti et al. (2015) vs. 0.33 Gyr from Chen et al. (2014)), so star age/ $\tau$  is either 1.6 or 16. Since the grains that can contribute significantly to the  $160\mu\text{m}$  emission have lifetimes against radiative drag of at least  $1/4$  the star age, they are likely to be destroyed by collisions before migrating significantly. Similarly, all systems have  $\beta < 0.05$  (where  $\beta = F_{\text{pr}}/F_g$ ;  $F_{\text{pr}}$  is the radiation pressure force given  $\langle Q_{\text{pr}}(a) \rangle = 1$  and  $F_g$  is the gravitational force) for  $25\mu\text{m}$  grains, so their orbits are not substantially modified by radiation pressure. The dust ring widths from our SED fits are likely close to the true widths of the

source planetesimal belts, with two caveats: (a) mutual grain collisions will increase the eccentricity dispersion and therefore the ring width (Thebault 2009), and (b) our models do not account for the possibility that the small grains have a wider spatial distribution than the large grains—we assume all grain sizes are well mixed throughout the dust annulus. In reality, radiation pressure might push the smallest grains to wide or eccentric orbits (Burns et al. 1979; Gáspár et al. 2012) and create structures similar to the  $\beta$  Pictoris, HR 8799, and HD 95086 “halos” seen in scattered light (Augereau et al. 2001; Su et al. 2009, 2015; Ballering et al. 2016). Pushing the small grains in the HD 105211 system to wider orbits might help resolve the conflict between the  $32/70\mu\text{m}$  flux ratio and the  $160\mu\text{m}$  flux density discussed in section 5.1. The HD 105211 disk also has the smallest  $a_{\text{min}}/a_{\text{rp}}$  size ratio of any disk in the sample, so is most likely to be affected by radiation pressure. Follow-up with ground-based adaptive optics or the Hubble Space Telescope could detect scattered light from blowout-size grains. If our *Herschel* photometry traces the birth rings, our systems can be added to the list of  $> 30$  debris disks with radii larger than the probable solar nebula radius of 80 AU (Kretke et al. 2012). Planetesimal formation seems to be a robust process even out to extremely large distances (Kenyon & Bromley 2012).

Finally, many lines of evidence suggest that at least some planetesimal belts are sculpted by planets (e.g. Quillen & Thorndike 2002; Chiang et al. 2009; Boley et al. 2012; Su & Rieke 2014; Sai et al. 2015). Interestingly, the disk surrounding HD 50554 is a true Kuiper Belt analog in its spatial distribution, with a best-fit radius of 45 AU and ring half-width of 4 AU. Since HD 50554 is slightly younger than the sun (3.3 Gyr; Bonfanti et al. 2015), its disk may be similar to the Kuiper Belt at an earlier stage of evolution and may have a Neptune-like planet at its inner edge. In N-body simulations of planetesimal belts with giant planets orbiting just inside their inner edges, Rodigas et al. (2014) find that the width of the planetesimal belt increases with both planet mass and planet/disk semimajor axes. Here we find that the width of the best-fit dust ring roughly increases with distance from the star, from  $\sigma = 4$  AU at  $R = 45$  AU for HD 50554 to  $\sigma = 20$  AU for both HD 202206 ( $R = 105$  AU) and HD 105211 ( $R = 175$  AU), though the width of the ring becomes less observationally constrained as  $R$  increases. However, we have no direct constraints on the presence or absence of planets on wide orbits, and we measure fractional dust luminosities of  $L_{\text{dust}}/L_* = 10^{-5} - 10^{-4}$  (Table 2), which are consistent with dust production from icy planetesimals stirred by Pluto-size dwarf planets Kenyon & Bromley (2010).

## 6. CONCLUSIONS AND FUTURE WORK

Here we have presented new *Herschel* and updated *Spitzer* photometry of five sunlike stars with debris disks of Kuiper Belt size and larger. Both extended structure in the images and SED fits from the Debris Disk Simulator (Wolf & Hillenbrand 2005) indicate that the disks are not composed of blackbody grains; instead, small grains are present and disks are wider than their blackbody radii. As seen by Booth et al. (2013), the minimum grain sizes in the best-fit SEDs are in the  $3.5\mu\text{m} - 4.5\mu\text{m}$  size range, larger than the radiation pressure blowout size.

All targets are younger than the sun (though still on the main sequence), so we may be seeing Kuiper Belt analogs at earlier phases of evolution. The disks have luminosities consistent with dust production from icy planetesimals stirred by Pluto-size bodies (Kenyon & Bromley 2010). We also find that the *Herschel*  $160\mu\text{m}$  emission likely emanates from the birth ring of planetesimals, so we add our targets to the growing list of Sunlike stars with planetesimals beyond the radius of the solar nebula. One caveat is that our SED models may not be unique: we assumed 100% astronomical silicate grains and did not consider mixtures of silicate, ice, and/or organic grains (though icy grain mantles will likely photo-evaporate). Another unexplored possibility is that different grain sizes have different radial distributions.

Although three of the stars host planets discovered by Doppler searches (HD 50554, HD 52265, and HD 202206), the planets are on short-period orbits that should be dynamically decoupled from the debris disks. Any planets that sculpt the debris disks in this sample have not yet been detected. HD 33636 has an M6 companion in a  $\sim 3$  AU orbit (Bean et al. 2007), indicating that the debris disk at 85 AU is circumbinary. HD 105211 may also be a spectroscopic binary, though Eggleton & Tokovinin (2008) find a single star more probable. HD 33636 and (possibly) HD 105211 complement  $\sim 30$  previous detections of circumbinary debris disks, though there is some indication that the frequency of cold debris disks may be higher among single stars (Rodríguez et al. 2015). There is no conclusive evidence that any of our targets host “holey” debris disks which have planets in the gaps (Kennedy & Wyatt 2014; Meshkat et al. 2015), though the IRS spectrum of HD 105211 may have a peak at  $19\mu\text{m}$  (see section 5.1).

Based on target declination, ALMA follow-up would be possible for HD 33636, HD 52265, HD 105211, and HD 202206. The most compelling target is HD 105211 due to both its brightness— $0.7$  Jy at  $100\mu\text{m}$ —and its spatial extent of  $> 14''$ , wider than the disk surrounding the T Tauri star TW Hydrae. HD 33636 and HD 52265 are also good ALMA targets based on their extended structure in the *Herschel* PACS images. We also suggest JWST follow-up of HD 105211 using the (a) the MIRI coronagraph with the  $23\mu\text{m}$  filter and (b) the MIRI low resolution spectrometer (LRS). Based on the allWISE W1 photometry, we find that the the Dodson-Robinson et al. (2011) photosphere model is likely accurate, which indicates that HD 105211 has a strong infrared excess at  $23\mu\text{m}$ . Observations with JWST would allow us to precisely locate the inner edge of the cold debris ring and possibly detect a hot inner debris belt, if it exists.

Funding for this work was provided by NASA research support agreement 1524391. We thank Roberta Paladini of the HASA *Herschel* Science Center for guidance on data reduction and Sebastian Wolf for developing the publicly available Debris Disk Simulator tool. John Gizis and Neal Evans provided helpful input on data analysis methods. This research has made use of the following resources: (1) *Herschel* Interactive Processing Environment (HIPE) and the *ipipe* scripts for data reduction. (2) VizieR catalogue access tool, CDS, Strasbourg, France. The original description of the VizieR service was published in A&AS 143, 23. (3) NASA/IPAC Infrared Science Archive, which is operated

by the Jet Propulsion Laboratory, California Institute of Technology, under contract with the National Aeronautics and Space Administration. (4) SIMBAD database, operated at CDS, Strasbourg, France;

Wenger et al. (2000). (5) *Herschel* Science Archive, [www.cosmos.esa.int/web/herschel/science-archive](http://www.cosmos.esa.int/web/herschel/science-archive). (6) `astropy` python library for astronomy, [www.astropy.org](http://www.astropy.org). (7) `APLpy` (Astronomical Plotting Library in Python), [aplpy.github.io](https://github.com/astropy/aplpy).

## REFERENCES

- Anderson, K. R., Adams, F. C., & Calvet, N. 2013, *ApJ*, 774, 9
- Ardila, D. R., Golimowski, D. A., Krist, J. E., et al. 2004, *ApJ*, 617, 147
- Augereau, J. C., Nelson, R. P., Lagrange, A. M., Papaloizou, J. C. B., & Mouillet, D. 2001, *A&A*, 370, 447
- Balling, N. P., Su, K. Y. L., Rieke, G. H., & Gáspár, A. 2016, *ApJ*, 823, 108
- Balog, Z., Müller, T., Nielbock, M., et al. 2014, *Experimental Astronomy*, 37, 129
- Bean, J. L., McArthur, B. E., Benedict, G. F., et al. 2007, *AJ*, 134, 749
- Beichman, C. A., Bryden, G., Stapelfeldt, K. R., et al. 2006, *ApJ*, 652, 1674
- Bessell, M. S. 1990, *A&AS*, 83, 357
- Bonfanti, A., Ortolani, S., Piotto, G., & Nascimbeni, V. 2015, *A&A*, 575, 18
- Boley, A. C., Payne, M. J., Corder, S., et al. 2012, *ApJ*, 750, 21
- Booth, M., Kennedy, G., Sibthorpe, B., et al. 2013, *MNRAS*, 428, 1263
- Bryden, G., Beichman, C. A., Carpenter, J. M., et al. 2009, *ApJ*, 705, 1226
- Burns, J. A., Lamy, P. L., & Soter, S. 1979, *Icarus*, 40, 1
- Chen, C. H., Mittal, T., Kuchner, M., et al. 2014, *ApJS*, 211, 25
- Chiang, E., Kite, E., Kalas, P., Graham, J. R., & Clampin, M. 2009, *ApJ*, 693, 734
- Cutri, R. M., et al. 2003, The IRSA 2MASS All-Sky Point Source Catalog, NASA/IPAC Infrared Science Archive, <http://irsa.ipac.caltech.edu/applications/Gator>
- Cutri, R. M., et al. 2013, VizieR Online Data Catalog: AllWISE Data Release (Cutri+ 2013). VizieR Data Catalog 2328
- Dodson-Robinson, S. E., Beichman, C. A., Carpenter, J. M., & Bryden, G. 2011, *AJ*, 141, 11
- Draine, B. T. 2006, *ApJ*, 636, 1114
- Duchêne, G., Arriaga, P., Wyatt, M., et al. 2014, *ApJ*, 784, 148
- Eggleton, P. P., & Tokovinin, A. A. 2008, *MNRAS*, 389, 869
- Eiroa, C., Fedele, D., Maldonado, J., et al. 2010, *A&A*, 518, L131
- Eiroa, C., Marshall, J. P., Mora, A., et al. 2013, *A&A*, 555, A11
- Gáspár, A., Psaltis, D., Özel, F., Rieke, G. H., & Cooney, A. 2012, *ApJ*, 749, 14
- Gáspár, A., & Rieke, G. H. 2014, *ApJ*, 784, 33
- Golimowski, D. A., Krist, J. E., Stapelfeldt, K. R., et al. 2011, *AJ*, 142, 30
- Gordon, K. D., Rieke, G. H., Engelbracht, C. W. 2005, *PASP*, 117, 503
- Gracia-Carpio, J., Wetzstein, M., Roussel, H., & the PACS Instrument Control Centre Team. 2015, [arXiv:1512.03252](https://arxiv.org/abs/1512.03252)
- Gray, R. O., Corbally, C. J., Garrison, R. F., et al. 2006, *AJ*, 132, 161
- Greaves, J. S., Holland, W. S., Moriarty-Schieven, G., et al. 1998, *ApJ*, 506, L133
- Hines, D. C., Schneider, G., Hollenbach, D., et al. 2007, *ApJ*, 671, L165
- Høg, E., Fabricius, C., Makarov, V. V., et al. 2000, *A&A*, 355, L27
- James, D. J. 2013, *PASP*, 125, 1087
- Kalas, P., Duchêne, G., Fitzgerald, M. P., & Graham, J. R. 2007, *ApJ*, 671, L161
- Kalas, P., Fitzgerald, M. P., & Graham, J. R. 2007, *ApJ*, 661, L85
- Kennedy, G. M., & Wyatt, M. C. 2014, *MNRAS*, 444, 3164
- Kenyon, S. J., & Bromley, B. C. 2010, *ApJS*, 188, 242
- Kenyon, S. J., & Bromley, B. C. 2013, *ApJ*, 143, 63
- Kenyon, S. J., & Bromley, B. C. 2015, *ApJ*, 806, 42
- Kenyon, S. J., & Bromley, B. C. 2016, *ApJ*, 817, 51
- Kretke, K. A., Levison, H. F., Buie, M. W., & Morbidelli, A. 2012, *AJ*, 143, 91
- Krist, J. E., Ardila, D. R., Golimowski, D. A., et al. 2005, *AJ*, 129, 1008
- Krist, J. E., Stapelfeldt, K. R., Bryden, G., et al. 2010, *AJ*, 140, 1051
- Krivov, A. V., Eiroa, C., Löhne, T., et al. 2013, *ApJ*, 772, 32
- Kurucz, R. L. 1992, in *IAU Symp. 149, The Stellar Populations of Galaxies*, ed. B. Barbuy & A. Renzini (Dordrecht: Kluwer), 225
- Laher, R. R., Gorjian, V., Rebull, L. M., et al. 2012, *PASP*, 124, 737
- Laor, A., & Draine, B. T. 1993, *ApJ*, 402, 441
- Liseau, R., Risacher, C., Brandeker, A., et al. 2008, *A&A*, 480, L47
- Lutz, D. 2010. PACS photometer point spread function. *Herschel Science Center, PICC-ME-TN-033, version 1.01*
- Matthews, B. C., Krivov, A. V., Wyatt, M. C., Bryden, G., & Eiroa, C. 2014, *Protostars and Planets VI*, 521
- McDonald, I., Zijlstra, A. A., & Boyer, M. L. 2012, *MNRAS*, 427, 343
- Meshkat, T., Bailey, V. P., Su, K. Y. L., et al. 2015, *ApJ*, 800, 5
- Morales, F. Y., Bryden, G., Werner, M. W., & Stapelfeldt, K. R. 2013, *ApJ*, 776, 111
- Ott, S. 2010, in *ASP Conf. Ser. 434, Astronomical Data Analysis Software and Systems XIX*, ed. Y. Mizumoto, K.-I. Morita, & M. Ohishi (San Francisco, CA: ASP), 139
- Pan, M., & Schlichting, H. E. 2012, *ApJ*, 747, 113
- Pawellek, N., & Krivov, A. V. 2015, *MNRAS*, 454, 3207
- Pawellek, N., Krivov, A. V., Marshall, J. P., et al. 2014, *ApJ*, 792, 65
- Perryman, M. A. C., et al. 1997, *A&A*, 323, L49
- Pilbratt, N. M., Riedinger, J. R., Passvogel, T., et al. 2010, *A&A*, 518, L1
- Popesso, P., Magnelli, B., Buttiglione, S., et al. 2012, [arXiv:1211.4257](https://arxiv.org/abs/1211.4257)
- Quillen, A. C., & Thorndike, S. 2002, *ApJ*, 578, L149
- Rodigas, T. J., Malhotra, R., & Hinz, P. M. 2014, *ApJ*, 780, 65
- Rodriguez, D. R., Duchêne, G., Henry, T., et al. 2015, *MNRAS*, 449, 3160
- Rodriguez, D. R., & Zuckerman, B. 2012, *ApJ*, 745, 147
- Saffe, C., Gómez, M., Pintado, O., & González, E. 2008, *A&A*, 490, 297
- Sai, S., Itoh, Y., Fukugawa, M., Shibai, H., & Sumi, T. 2015, *PASJ*, 67, 20
- 2006, *ApJ*, 648, 652
- Su, K. Y. L., Morrison, S., Malhotra, R., et al. 2015, *ApJ*, 799, 146
- Su, K. Y. L., & Rieke, G. 2014, *Exploring the Formation and Evolution of Planetary Systems*, 299, 318
- Su, K. Y. L., Rieke, G. H., Stapelfeldt, K. R., et al. 2009, *ApJ*, 705, 314
- Su, K. Y. L., Rieke, G., Stapelfeldt, K., et al. 2010, *BAAS*, 42, 349
- Thébaud, P. 2009, *A&A*, 505, 1269
- Trilling, D. E., Bryden, G., Beichman, C. A., et al. 2008, *ApJ*, 674, 1086
- van Leeuwen, F. 2007, *Astrophysics and Space Science Library*, vol. 350
- van Leeuwen, F. 2007, *A&A*, 474, 653
- Wenger, M., Ochsenbein, F., Egret, D., et al. 2000, *A&AS*, 143, 9
- Wolf, S. 2003, *Computer Physics Communications*, 150, 99
- Wolf, S., & Hillenbrand, L. A. 2005, *Computer Physics Communications*, 171, 208
- Wright, E. L., Eisenhardt, P. R. M., Mainzer, A. K., et al. 2010, *AJ*, 140, 1868
- Wyatt, M. C., Clarke, C. J., & Booth, M. 2012, *Celestial Mechanics and Dynamical Astronomy*, 111, 1
- Wyatt, M. C., Greaves, J. S., Dent, W. R. F., & Coulson, I. M. 2005, *ApJ*, 620, 492

TABLE 1  
PHOTOMETRY

Instrument	Wavelength	Analysis Method	HD 33636	HD 50554	HD 52265	HD 105211	HD 202206
MIPS	24 $\mu$ m	Chen et al. (2014)	43.9 $\pm$ 0.9 <sup>a,b</sup>	51.0 $\pm$ 1.0 <sup>b</sup>	76.4 $\pm$ 1.5 <sup>b</sup>	367.9 $\pm$ 22.5 <sup>c</sup>	...
MIPS	24 $\mu$ m	Su et al. (2010)	42.5 $\pm$ 0.5	48.6 $\pm$ 0.5	76.2 $\pm$ 0.8	374.6 $\pm$ 3.8	...
MIPS	70 $\mu$ m	Chen et al. (2014)	35.0 $\pm$ 2.7 <sup>d</sup>	42.0 $\pm$ 4.5 <sup>d</sup>	38.0 $\pm$ 5.4 <sup>d</sup>	473.7 $\pm$ 19.8 <sup>c</sup>	28.9 $\pm$ 3.4 <sup>e</sup>
MIPS	70 $\mu$ m	Su et al. (2010)	38.1 $\pm$ 2.4	43.5 $\pm$ 3.0	40.5 $\pm$ 6.0	702 $\pm$ 38	27.9 $\pm$ 3.4
PACS	70 $\mu$ m	this work	...	48.1 $\pm$ 4.3	40.3 $\pm$ 5.5	692.0 $\pm$ 52.6	33.1 $\pm$ 3.7
PACS	100 $\mu$ m	this work	42.5 $\pm$ 6.1	39.5 $\pm$ 10.0	37.3 $\pm$ 11.1	704.0 $\pm$ 95.1	43.4 $\pm$ 4.9
PACS	160 $\mu$ m	this work	30.4 $\pm$ 10.2	23.7 $\pm$ 8.8 <sup>f</sup>	undetected	440.3 $\pm$ 146.0	36.1 $\pm$ 7.5

<sup>a</sup> Flux density units are mJy. Photometry has not been color-corrected.

<sup>b</sup> Original source: IPAC IRSA Spitzer Enhanced Imaging Products Catalog, [irsa.ipac.caltech.edu/data/SPITZER/Enhanced/Imaging](http://irsa.ipac.caltech.edu/data/SPITZER/Enhanced/Imaging)

<sup>c</sup> Original source: Beichman et al. (2006)

<sup>d</sup> Original source: Trilling et al. (2008)

<sup>e</sup> Original source: Bryden et al. (2009)

<sup>f</sup> Detection significance is between  $2\sigma$  and  $3\sigma$ .

TABLE 2  
DUST RING PARAMETERS FROM SED FITS AND IMAGES

Star	$R_{\text{SED}}$ (AU) <sup>a</sup>	$\sigma$ (AU) <sup>b</sup>	$a_{\text{min}}$ ( $\mu$ m) <sup>c</sup>	$M_{\text{dust}}$ ( $M_{\odot}$ ) <sup>d</sup>	$T_{\text{BB}}$ (K) <sup>e</sup>	$R_{\text{BB}}$ (AU) <sup>f</sup>	$\Gamma^g$	$L_{\text{dust}}/L_{\star}^h$
HD 33636	85	12	3.0	$10^{-8}$	46	37	2.3	$5.4 \times 10^{-5}$
HD 50554	45	4	4.5	$3 \times 10^{-9}$	59	27	1.7	$4.1 \times 10^{-5}$
HD 52265	70	10	3.0	$3 \times 10^{-9}$	58	32	2.2	$2.0 \times 10^{-5}$
HD 105211	175	20	4.1	$6.6 \times 10^{-8}$	49	86	2.0	$5.4 \times 10^{-5}$
HD 202206	105	20	3.0	$4 \times 10^{-8}$	45	40	2.7	$1.3 \times 10^{-4}$

<sup>a</sup> Distance of the center of the dust ring from the star, computed from SED

<sup>b</sup> Half-width of debris ring, assuming Gaussian number density profile for dust

<sup>c</sup> Minimum grain size

<sup>d</sup> Dust mass

<sup>e</sup> Temperature of dust grains, assuming blackbody emission

<sup>f</sup> Radius of disk of blackbody grains

<sup>g</sup>  $R/R_{\text{BB}}$

<sup>h</sup> Ratio of dust luminosity to star luminosity

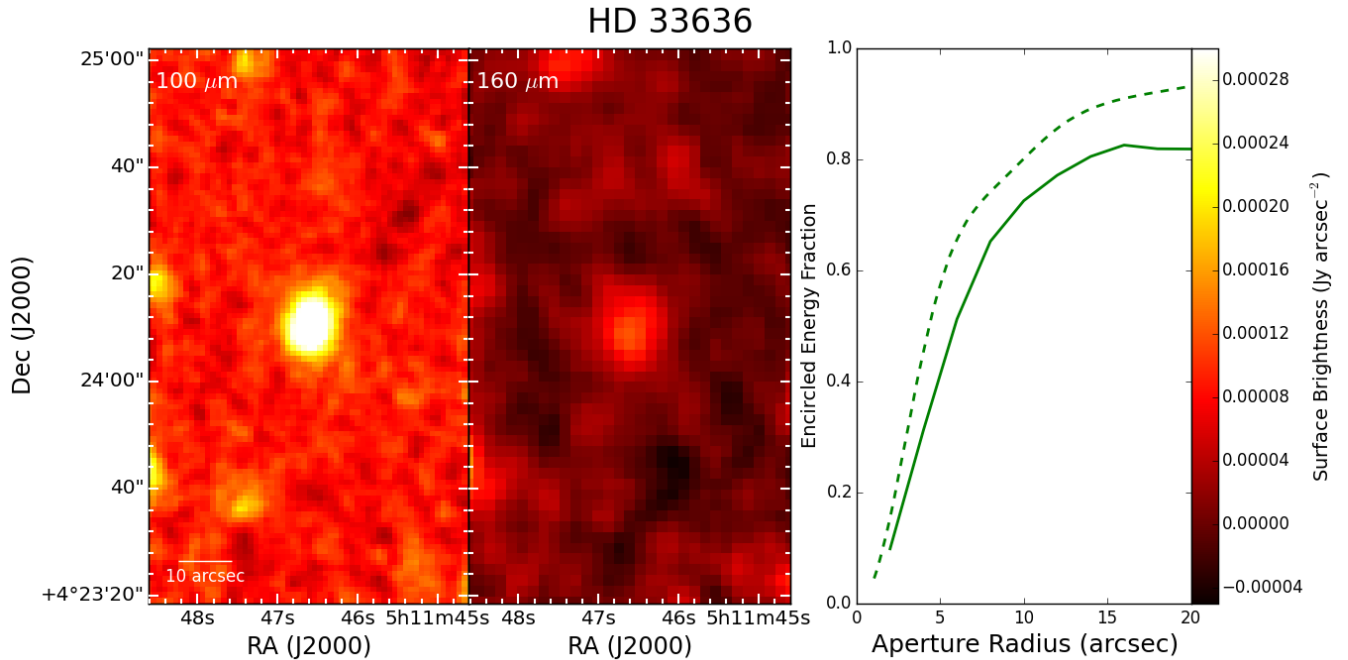


FIG. 1.— PACS images of HD 33636. The rightmost panel shows 100 $\mu$ m curves of growth for the point source Vesta (dashed line) and HD 33636 (solid line). Encircled energy fraction rises more slowly with aperture radius for HD 33636 than for Vesta, indicating that HD 33636 is extended at 100 $\mu$ m.



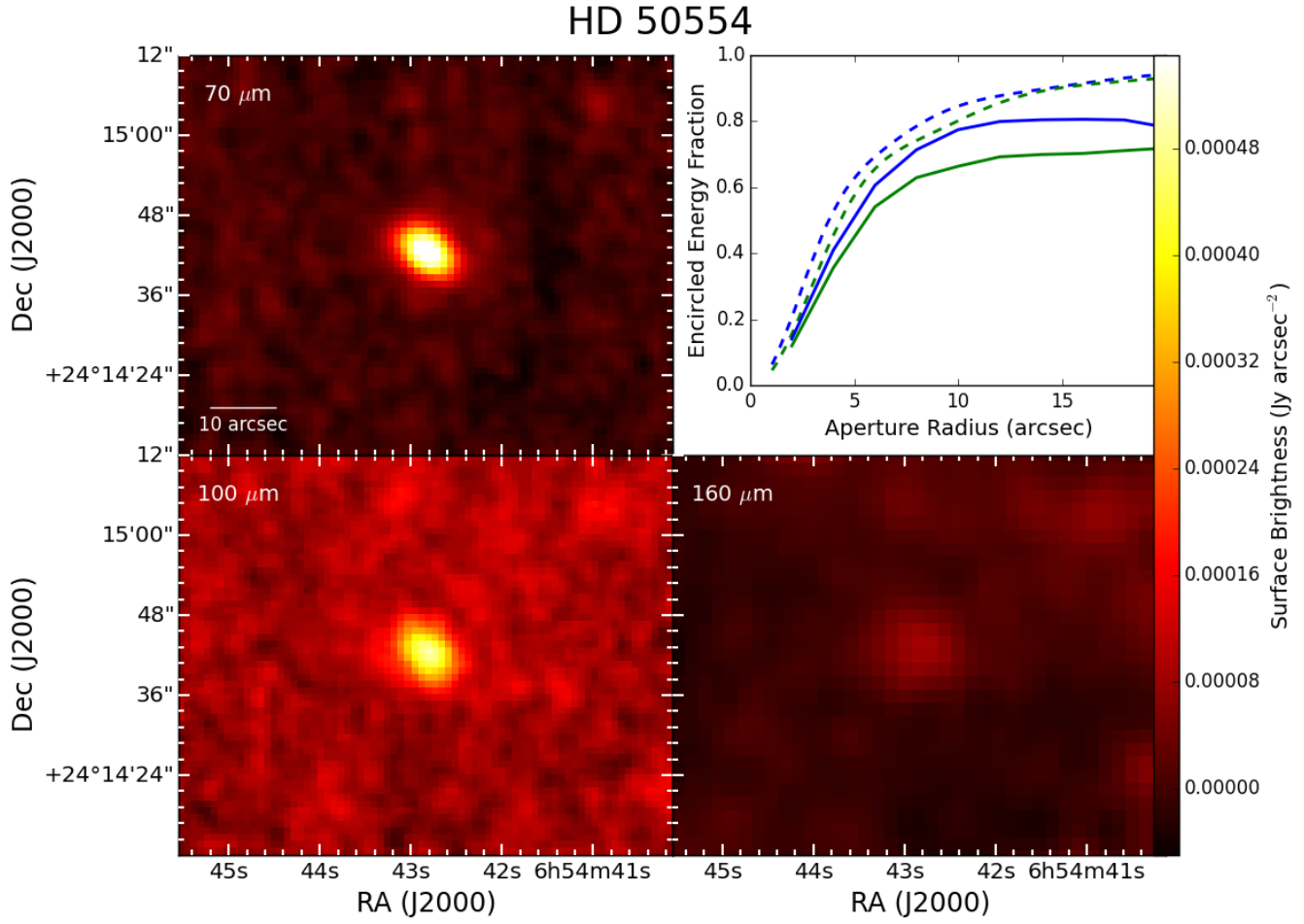


FIG. 2.— PACS images of HD 50554. The upper-right plot shows curves of growth for the point source Vesta (dashed lines) and HD 50554 (solid lines), with  $70\ \mu\text{m}$  in blue and  $100\ \mu\text{m}$  in green. The slower rise of HD 50554's curves of growth compared with Vesta's indicates extended structure, which is clearly visible in the  $70\ \mu\text{m}$  and  $100\ \mu\text{m}$  images.

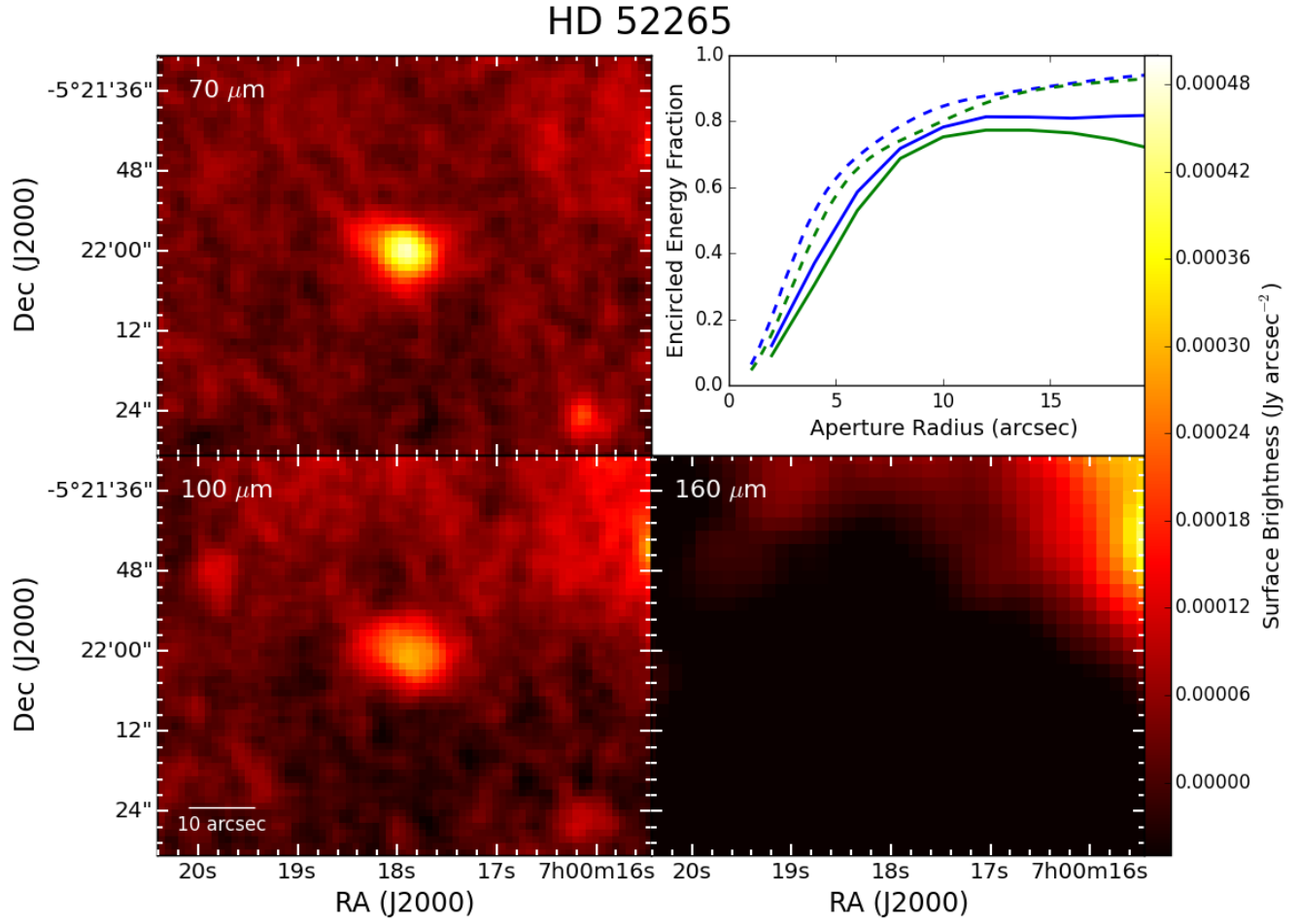


FIG. 3.— PACS images of HD 52265. The upper-right plot shows curves of growth for the point source Vesta (dashed lines) and HD 52265 (solid lines), with 70  $\mu\text{m}$  in blue and 100  $\mu\text{m}$  in green. Curves of growth suggest extended structure in the 70  $\mu\text{m}$  and 100  $\mu\text{m}$  images, though the background confusion may mimic extended structure. Confusion noise prevents detection of HD 52265 at 160  $\mu\text{m}$ .

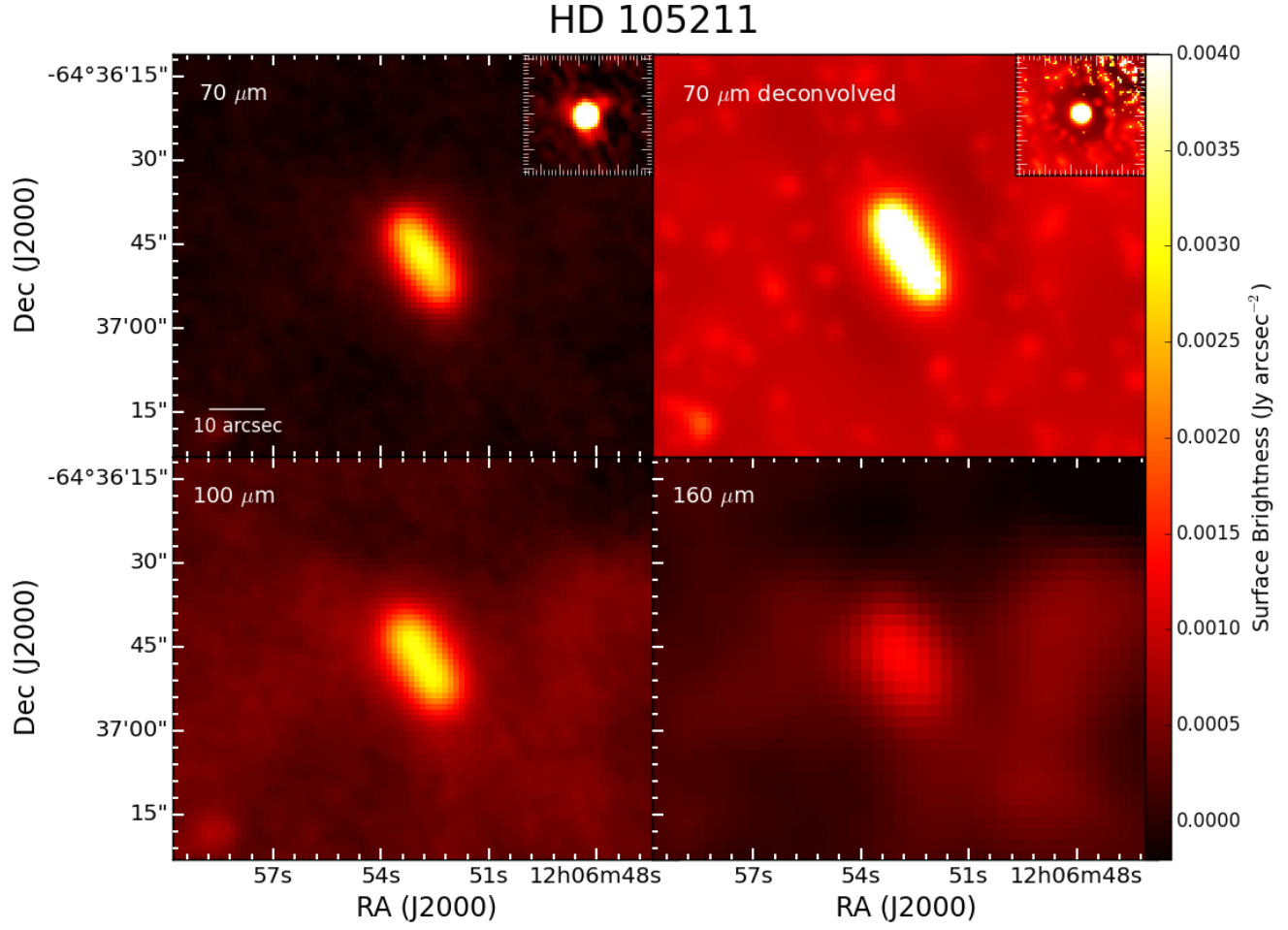


FIG. 4.— PACS images of HD 105211. The disk is well resolved at all PACS wavelengths. The deconvolved  $70\mu\text{m}$  image in the upper-right panel was created using the PSF measured from a point source in the  $70^\circ$  cross-scan. The insets in the  $70\mu\text{m}$  plot panels show the point source before deconvolution (left), with the tri-lobe structure visible, and after deconvolution (right).

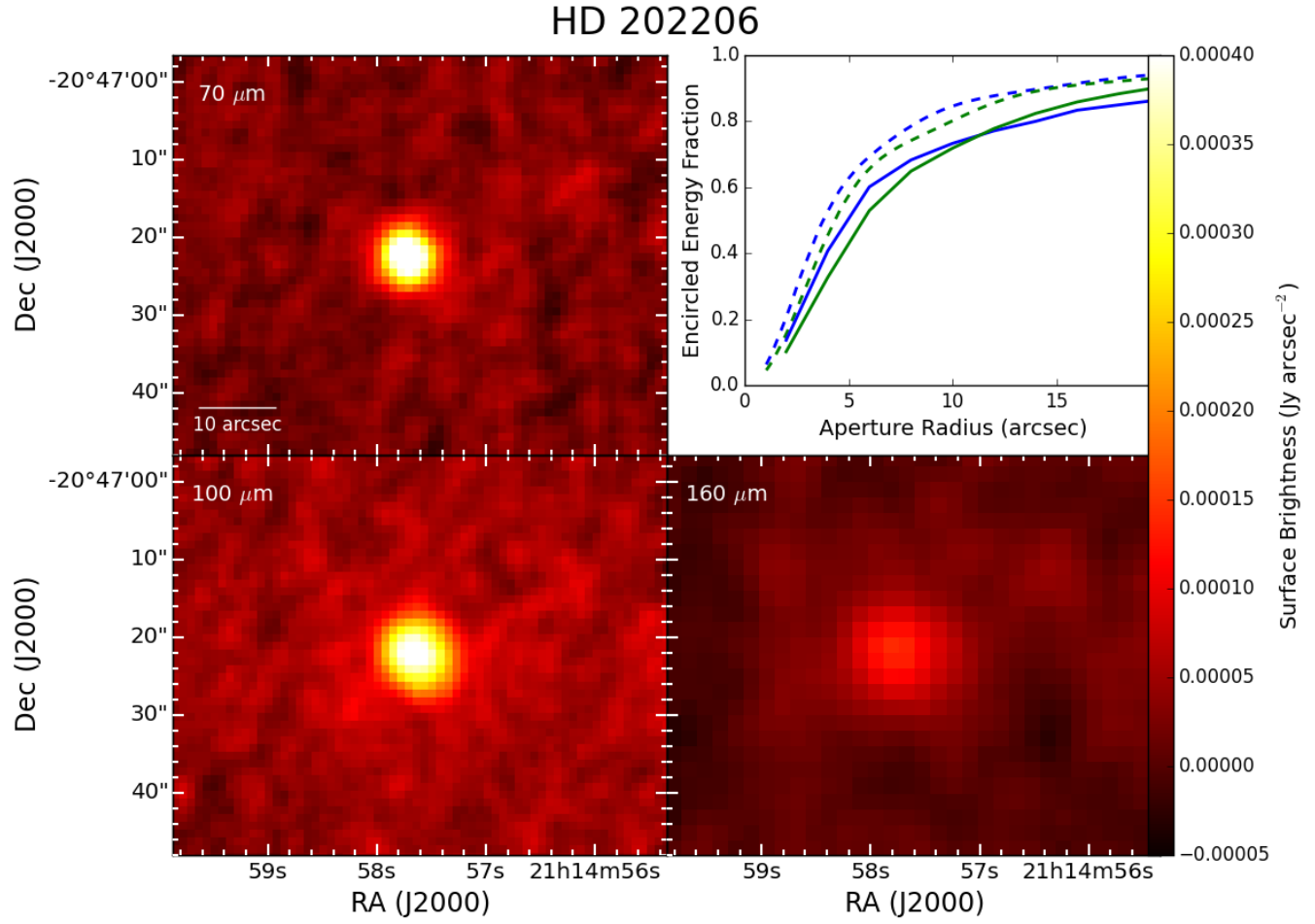


FIG. 5.— PACS images of HD 202206. 70 $\mu\text{m}$  and 100 $\mu\text{m}$  curves of growth do not conclusively show extended structure.

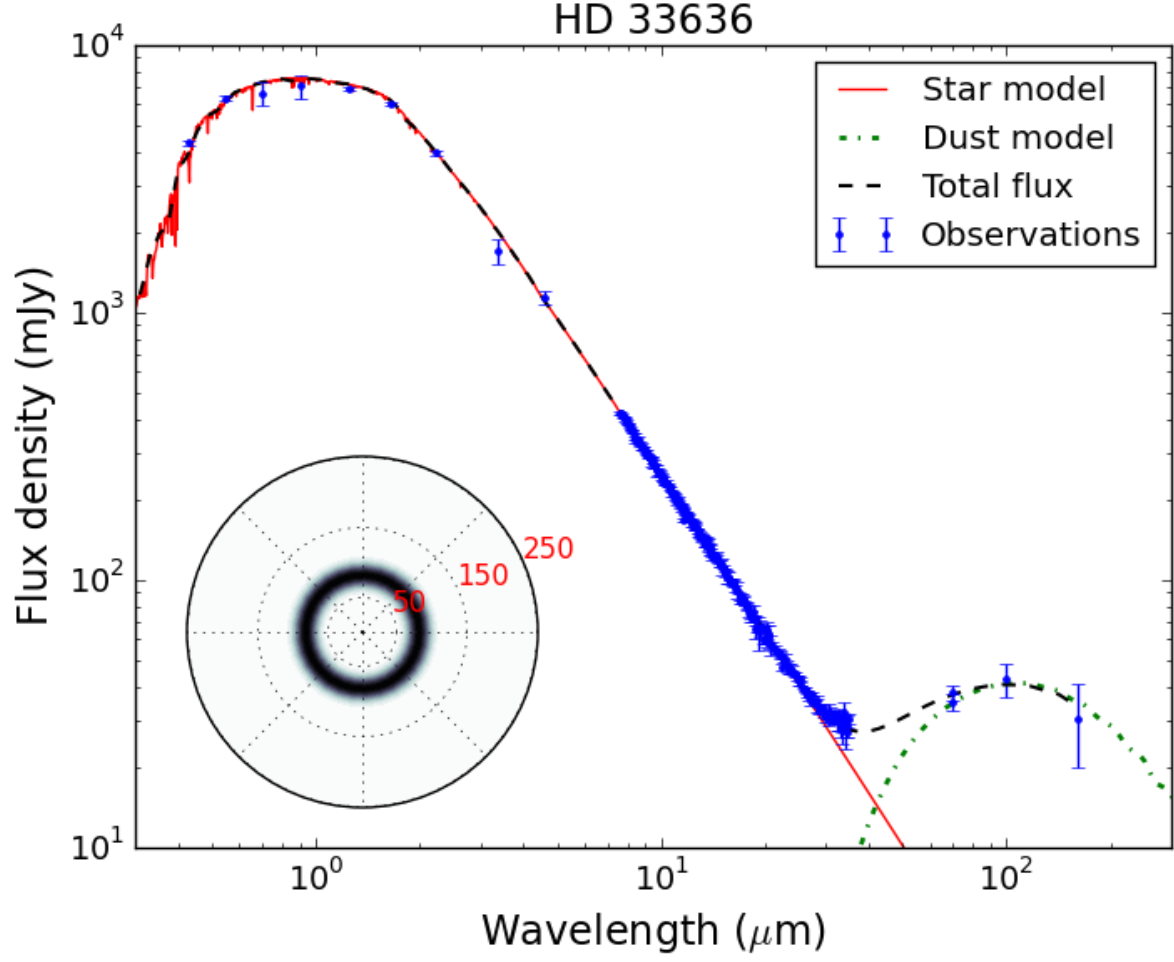


FIG. 6.— Spectral energy distribution of the HD 33636 star-disk system. The inset plot at the lower left shows the best-fit dust ring model, which is centered at 85 AU and has width 12 AU. Observational data include Hipparcos  $BV$ ,  $RI$  from Bessell (1990), 2MASS  $JHK$ , allWISE, *Spitzer* IRS and MIPS, and PACS 100/160 $\mu\text{m}$ .

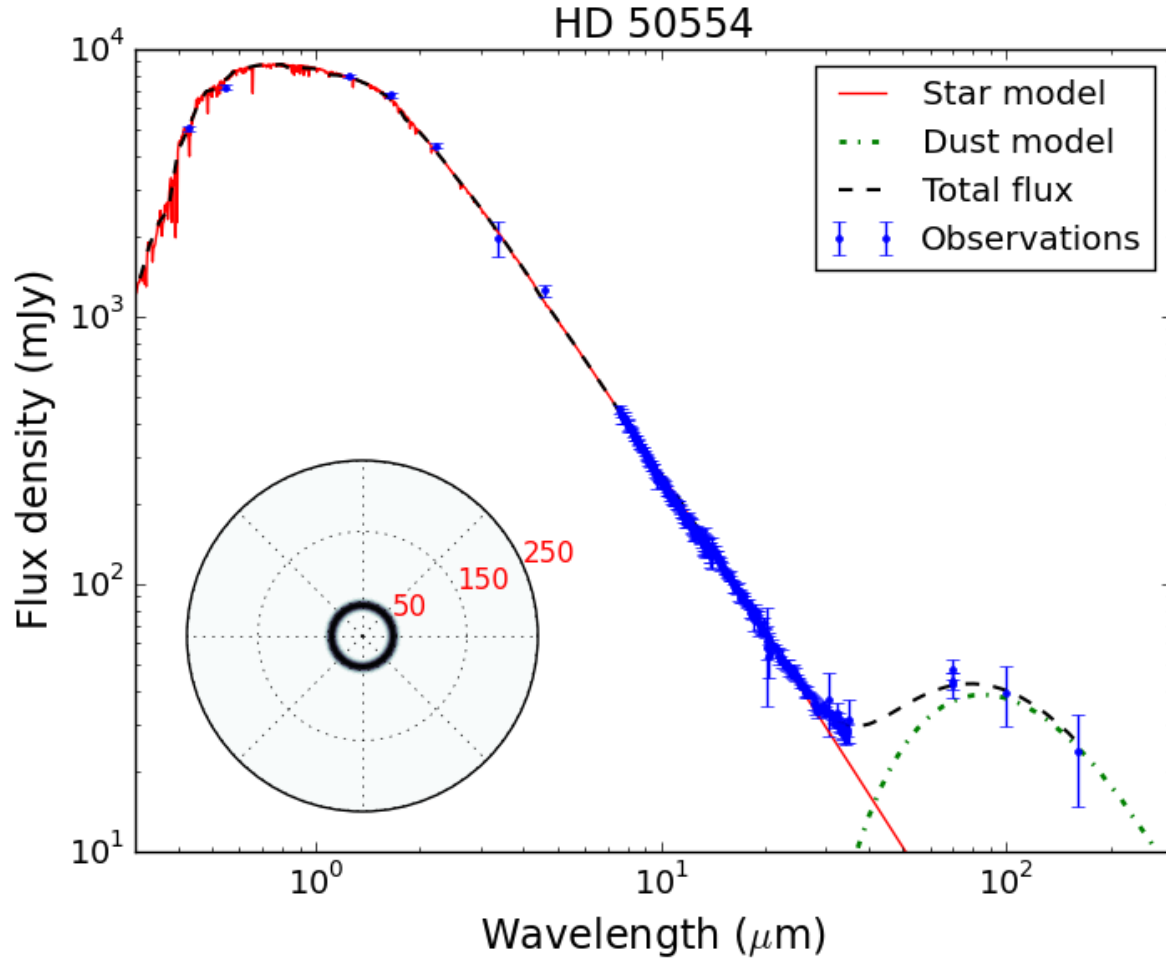


FIG. 7.— Spectral energy distribution of the HD 50554 star-disk system. The lower-left inset shows the best-fit Gaussian ring model with center 45 AU and width 4 AU. Observational data include Hipparcos *BV*, 2MASS *JHK*, allWISE, *Spitzer* IRS and MIPS, and *Herschel* PACS.

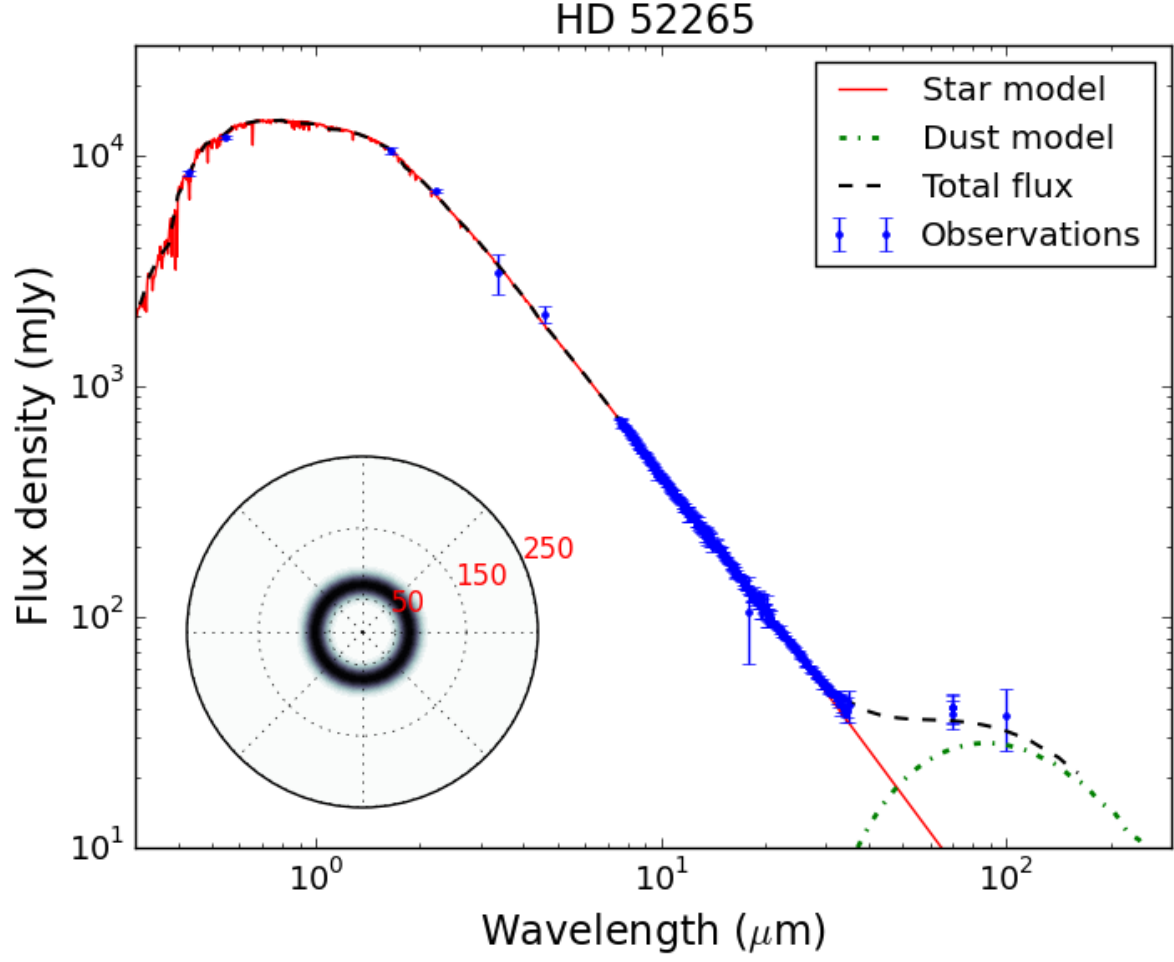


FIG. 8.— Spectral energy distribution of the HD 52265 star-disk system. The lower-left inset shows the best-fit Gaussian ring model with center 70 AU and width 10 AU. Observational data include Hipparcos *BV*, 2MASS *HK*, allWISE, *Spitzer* IRS and MIPS, and *Herschel* PACS. HD 52265 was not detected at  $160\mu\text{m}$ . 2MASS *J* photometry was flagged as low quality and was not included in the analysis.

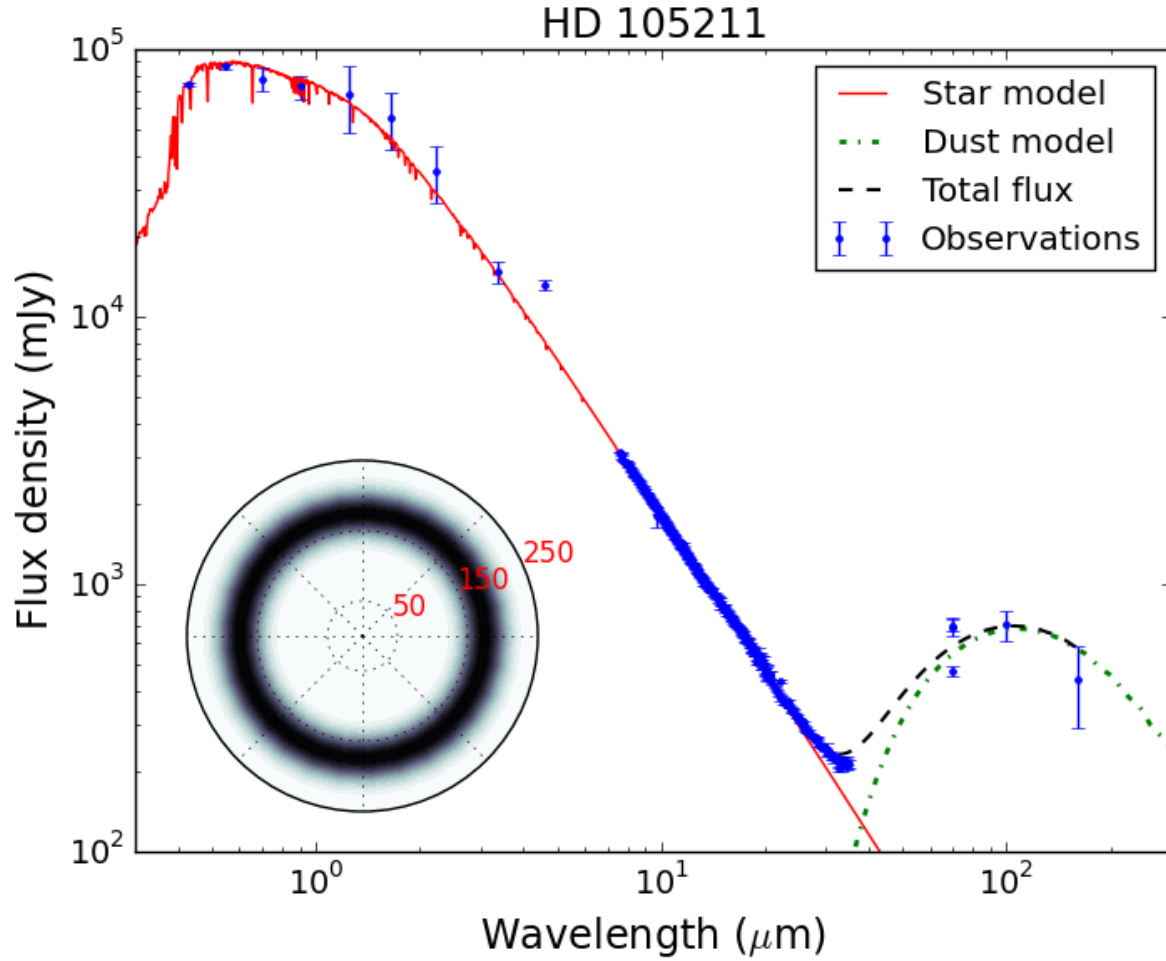


FIG. 9.— Spectral energy distribution of the HD 105211 star-disk system. The lower-left inset shows the best-fit Gaussian ring model with center 175 AU and width 20 AU. Observational data include Hipparcos *BV*, Bessell (1990) *RI*, 2MASS *JHK*, allWISE, *Spitzer* IRS and MIPS, and *Herschel* PACS. HD 105211 is saturated in the allWISE W2 filter.



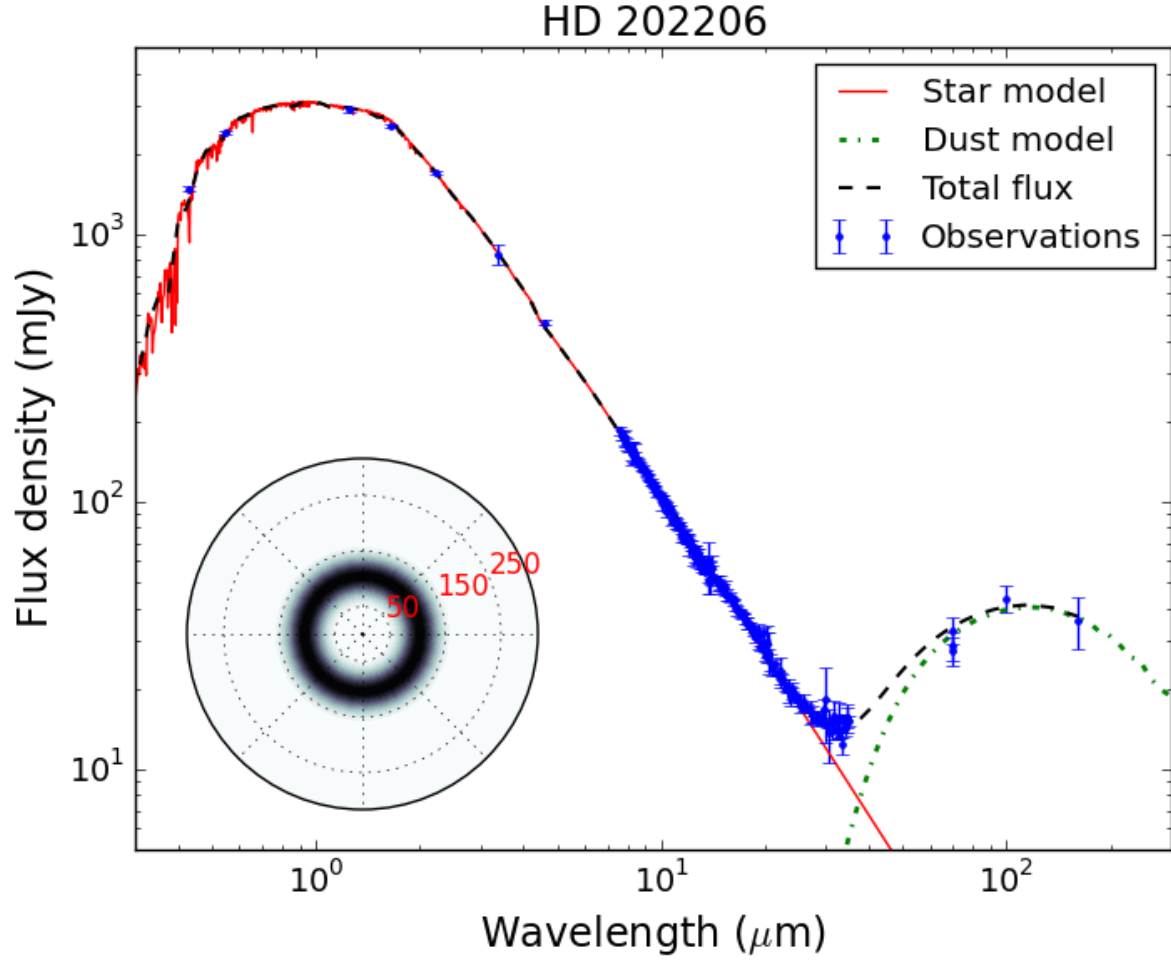


FIG. 10.— Spectral energy distribution of the HD 202205 star-disk system. The lower-left inset shows the best-fit Gaussian ring model with center 105 AU and width 20 AU. Observational data include Hipparcos *BV*, 2MASS *JHK*, allWISE, *Spitzer* IRS and MIPS, and *Herschel* PACS.

TABLE 3  
TARGET STARS

HD	Name	Spectral Type	$V$ (mag) <sup>a</sup>	$d_*$ (pc) <sup>b</sup>	$L_*/L_\odot$ (this work)	$L_*/L_\odot$ (literature) <sup>c</sup>	Age (Gyr) <sup>c</sup>	Observation IDs <sup>d</sup>
33636		G0VH-03	7.06	28.7	1.05	1.08	2.5	134226927[2/3]
50554		F8V	6.84	31.0	1.51	1.37	3.3	134223115[2/3], 134226899[6/7], 134226899[8/9]
52265		G0V	6.30	28.1	2.04	2.08	2.6	134223156[4/5], 134226925[8/9]
105211	$\eta$ Cru	F2V	4.15	19.7	7.31	7.06 <sup>e</sup>	1.4 <sup>f</sup>	134226237[1/2], 134226237[3/4]
202206		G6V	8.08	46.3	1.07	1.02	1.1	134221939[7/8], 134223168[6/7]

<sup>a</sup>  $V$  magnitudes were obtained from color transformations of the Tycho-2  $V_T$  photometry (Høg et al. 2000).

<sup>b</sup> Distances come from the Hipparcos reduction of van Leeuwen (2007a,b).

<sup>c</sup> Luminosities and ages from Bonfanti et al. (2015) unless otherwise indicated.

<sup>d</sup> Observation IDs recorded in Herschel Science Archive v7.1.1. Notation: 134226927[2/3] = cross-scan pair of 1342269272 and 1342269273.

<sup>e</sup> Luminosity from McDonald et al. (2012).

<sup>f</sup> Age from Chen et al. (2014).